Contents lists available at ScienceDirect

International Journal of Biological Macromolecules

journal homepage: www.elsevier.com/locate/ijbiomac

Silk fibroin nanoparticles for locoregional cancer therapy: Preliminary biodistribution in a murine model and microfluidic GMP-like production

Francesca Ferrera [a,1], Roberta Resaz [b,1], Elia Bari [c,*], Daniela Fenoglio [a,d], Luca Mastracci [e,f], Ivana Miletto [c], Angelo Modena [c], Sara Perteghella [g,h], Marzio Sorlini [h,i], Lorena Segale [c], Gilberto Filaci [a,d], Maria Luisa Torre [c,h], Lorella Giovannelli [c]

[a] *Department of Internal Medicine, Centre of Excellence for Biomedical Research, University of Genoa, Viale Benedetto XV 6, 16132 Genova, Italy*
[b] *Animal Facility, IRCCS Ospedale Policlinico San Martino, Largo R. Benzi 10, 16132 Genova, Italy*
[c] *Department of Pharmaceutical Sciences, University of Piemonte Orientale, Largo Donegani 2/3, 28100 Novara, Italy*
[d] *Biotherapy Unit, IRCCS Policlinico San Martino, Largo R. Benzi 10, 16132 Genova, Italy*
[e] *Department of Surgical and Integrated Diagnostic Sciences, University of Genoa, Viale Benedetto XV 6, 16132 Genova, Italy*
[f] *Anatomic Pathology Unit, IRCCS Ospedale Policlinico San Martino, Largo R. Benzi 10, 16132 Genova, Italy*
[g] *Department of Drug Sciences, University of Pavia, Via Taramelli 12, 27100 Pavia, Italy*
[h] *PharmaExceed s.r.l., Piazza Castello 19, 27100 Pavia, Italy*
[i] *Department of Innovative Technologies, University of Applied Sciences and Arts of Southern Switzerland, SUPSI, Lugano University Centre, Campus Est, Via la Santa 1, CH-6962 Viganello, Switzerland*

ARTICLE INFO

ABSTRACT

Silk fibroin nanoparticles (SFNs) have been widely investigated for drug delivery, but their clinical application still faces technical (large-scale and GMP-compliant manufacturing), economic (cost-effectiveness in comparison to other polymer-based nanoparticles), and biological (biodistribution assessments) challenges. To address biodistribution challenge, we provide a straightforward desolvation method (in acetone) to produce homogeneous SFNs incorporating increasing amounts of Fe_2O_3 (SFNs-Fe), detectable by Magnetic Resonance Imaging (MRI), and loaded with curcumin as a model lipophilic drug. SFNs-Fe were characterized by a homogeneous distribution of the combined materials and showed an actual Fe_2O_3 loading close to the theoretical one. The amount of Fe_2O_3 incorporated affected the physical-chemical properties of SFNs-Fe, such as polymer matrix compactness, mean diameter and drug release mechanism. All formulations were cytocompatible; curcumin encapsulation mitigated its cytotoxicity, and iron oxide incorporation did not impact cell metabolic activity but affected cellular uptake in vitro. SFNs-Fe proved optimal for biodistribution studies, as MRI showed significant nanoparticle retention at the administration site, supporting their potential for locoregional cancer therapy. Finally, technical and economic challenges in SFN production were overcome using a GMP-compliant microfluidic scalable technology, which optimized preparation to produce smaller particle sizes compared to manual methods and reduced acetone usage, thus offering environmental and economic benefits. Moreover, enabling large-scale production of GMP-like SFNs, this represents a considerable step forward for their application in the clinic.

1. Introduction

In biomedical research, nanostructured materials are garnering increased attention for their potential applications in therapy, diagnostic, and imaging [1]. Among them, silk fibroin (SF)-nanoparticles (SFNs) are of particular interest as a chemotherapeutic delivery platform, especially in cancer treatment. SF is a popular choice for nanoparticle formulation due to its remarkable mechanical properties [2], biocompatibility [3–5], biodegradability [6,7], and functional groups that lend themselves to functionalization [8–14]. SFNs also offer optimal entrapment, great binding affinities (and thus remarkable cell uptake) [15], and enhanced therapeutic index for different cytotoxic

---

* Corresponding author.
  E-mail address: elia.bari@uniupo.it (E. Bari).
[1] Equally contributed.

drugs [14,16]. For all these reasons, SFNs represent a good strategy for the passive or active delivery of a drug to targeted cancer cells, and recently, they were applied to a protocol of cancer immunotherapy as a tool for delivering an antigen into a tumor to recall against it a pre-existing immunity [17]. Studies have found that the enhanced permeability and retention (EPR) effect, which capitalizes on abnormal blood vessels and impaired drainage in the tumor microenvironment, justified the accumulation of nanoparticles in tumors [18]. Furthermore, the functionalization of the SFN surface can enable active targeting so that the uptake is selective only by tumor cells, hence confirming minimal harm to healthy nearby cells [8,10–14].

However, despite the potential of SFNs in cancer therapy, which has sparked considerable interest in the biomedical research community, and ongoing investigations continue to explore their capabilities and refine their applications, several obstacles must be overcome to guarantee clinical efficacy in translating laboratory experimentation to practical application. These include (i) technical issues, such as large-scale and GMP-compliant manufacturing, process control, and batch reproducibility; (ii) economic issues, e.g., overall cost-effectiveness in comparison to nanoparticles based on other polymers; and (iii) biological issues, including biodistribution assessments, biocompatibility, biodegradation and safety [19].

Regarding technical challenges, production methods must reproducibly generate SFNs with uniform properties. In past practices, the production of SFNs has mainly relied on bulk mixing techniques, which often resulted in unpredictable variations in the levels of reactants, leading to inconsistent, polydisperse particles [20]. In addition, the use of batch methods also poses a risk of damaging the enclosed components or substances due to the energies required to mix reagents within the reaction vessel [21]. Such limitations can be overcome through microfluidic techniques, where the parameters can be tightly controlled to consistently produce particles of the desired size and characteristics without damaging the cargo [22]. This approach is useful to control particle dimensions, reduce size dispersion, improve functionalization, and increase run-to-run reproducibility [23]. On the other hand, if the microfluidic protocol has to represent an advantageous chance, it is mandatory to consider the regulatory standards and good manufacturing practice (GMP) because they are essential for the incorporation of these new technologies in the production of therapeutic products.

Regarding biological challenges, the regulatory approval of these nanosystems depends on the biodistribution of SFNs, which cannot be easily evaluated without proper functionalization with imaging probes. In this regard, a strategy relevant also to theranostic applications is combining SF with other materials to obtain multifunctional nanocomposites [24] with new tailored physical properties. For example, iron oxide (Fe_2O_3) loaded SFNs may be a useful tool in Magnetic Resonance Imaging (MRI) because iron oxide reduces the T2 (or transverse) relaxation time of neighboring water protons that appear darker [25–29]; moreover, due to iron oxide superparamagnetic property, in loco magnetic hyperthermia occurs [30–34]. As a result, it will be possible to monitor the circulation and biodistribution of SFNs, to target tissues selectively due to their nanosize or functionalization with targeting agents, to deliver a sufficient amount of drug, and further treat tumors exploiting the hyperthermia related to superparamagnetic properties [35]. The literature already reports the combination of SF with Fe_2O_3 to generate, for example, microspheres [24] or scaffolds [36]. Only Deng and colleagues proposed core-shell nanoparticles, in which iron oxide was in the core, and the shell was made of SF. The cell uptake was facilitated by the coating of the systems with SF and, at the same time, hampered by the shape (cubic) of the produced particles [37]. None of these studies evaluated the potential of SF and Fe_2O_3 composites for theranostic applications or investigated the different behavior of SF in the presence of iron oxide.

Given these premises, here we aim to overcome some of the technical, economic, and biological challenges mentioned above.

Table 1
Theoretical composition of the formulations prepared.

Formulation	SF *w/w* %	Curcumin *w/w* %	Fe_2O_3 *w/w* %
SFNs-CUR	77.6	22.4	–
A	76.7	22.2	1.1
B	76.0	21.9	2.1
C	74.7	21.6	3.7
D	72.0	20.8	7.2

Specifically, regarding the biological challenges, for the biodistribution assessment, we provide a powerful yet straightforward desolvation method (in acetone) to produce homogeneous SFNs incorporating Fe_2O_3 (SFNs-Fe) and curcumin as a lipophilic drug model. Different formulations, prepared by increasing the amount of incorporated Fe_2O_3, were fully characterized concerning particle size and size distribution, physical-chemical properties, morphology, and ultrastructure. This allowed us to understand, for the first time to the best of our knowledge, how the amount of Fe_2O_3 changes the behavior of SF following the desolvation process. Furthermore, all the formulations were in vitro tested to demonstrate cytocompatibility and proper cell uptake, and, for the first time, in vivo administered to evaluate their capability to decrease signal intensity in MRI. Last, to overcome technical challenges, the preparation procedure of SFNs was optimized using a GMP-compliant and scalable microfluidic technology, and the characteristics of the obtained nanoparticles were compared to those produced in bulk mixing. The use of GMP microfluidic also allowed for the reduction of the amount of organic solvent used and, thus, improved the economic and environmental sustainability of SFNs as drug delivery systems.

2. Materials and methods

2.1. Materials and reagents

3-(4,5-Dimethylthiazol-2-yl)-2,5-diphenyltetrazolium bromide (MTT), curcumin, lithium bromide (LiBr), mannitol, and sodium carbonate (Na_2CO_3) were supplied by Merck, Milan, Italy. Acetone, dimethyl sulphoxide (DMSO), and ethanol were purchased from Carlo Erba Reagents, Milan, Italy. Cell culture media, antibiotics, and fetal bovine serum (FBS) were purchased from Biosigma, Cona (VE), Italy. Fe_2O_3 nanopowder was kindly donated by TEC Star Srl, Castelfranco Emilia (MO), Italy, while *Bombyx mori* cocoons were donated by Nembri industrie tessili, Capriolo (BS), Italy. Dialysis tubes were purchased from Spectrum Laboratories, Milan, Italy.

2.2. Preparation and characterization of silk fibroin nanoparticles incorporating Fe_2O_3 (SFNs-Fe)

2.2.1. Silk fibroin nanoparticles preparation

SF was extracted from *Bombyx mori* cocoons, and its solution in LiBr 9.3 M was prepared according to the method described in a previous work [38].

The desolvation method with acetone was used for the preparation of SFNs. First, Fe_2O_3 nanopowder was added to SF diluted aqueous solution (1.5 % *w/v*) in increasing amounts to reach the Fe_2O_3:SF ratios of 1:80, 1:40, 1:20, and 1:10; after thoughtful mixing, the final mixture was added dropwise to the acetone (1:5 ratio) where curcumin was solubilized at 0.8 mg/mL. SFNs-CUR were prepared without mixing SF with iron oxide. The theoretical composition for each formulation prepared is reported in Table 1. All SFNs were dialyzed for 72 h using dialysis cellulose tubes and freeze-dried ($T = -50\ °C$, $P = 8 \times 10^{-1}$ mbar for 72 h, Epsilon 2-6D LSCplus, Martin Christ GmbH, Osterode am Harz, Germany) using 0.5 % *w/v* mannitol as a cryoprotectant to facilitate the dispersion of freeze-dried powders. The samples were stored at room temperature until use (up to 2 months). Three batches of each formulation were prepared and characterized.

2.2.2. Production yield, encapsulation efficiency and drug loading

For all the SFNs prepared, the production yield (Y%) was calculated according to Eq. (1):

$$Y\% = \frac{SFNs\ (g)}{W\ SF\ (g) + W\ curcumin(g) + W\ iron\ oxide(g)} \times 100 \qquad (1)$$

All the freeze-dried SFNs were dispersed in 96 % *v/v* ethanol (0.1 mg/mL) under mild magnetic stirring in the dark for 72 h to evaluate the curcumin loading. The supernatants were analyzed spectrophotometrically (Victor Nivo, PerkinElmer, Waltham, MA, USA) at 425 nm, using ethanol as blank, and the drug concentration was determined referring to a calibration curve built in the curcumin concentration range 0.25–10 μg/mL ($R^2 = 0.989$). Eq. (2) was used to calculate the drug loading (D% *w/w*):

$$D\% = \frac{total\ curcumin\ amount}{total\ amount\ of\ SFNs} \times 100 \qquad (2)$$

Finally, the encapsulation efficiency (EE%) was determined as follows:

$$EE\% = \frac{actual\ entrapped\ curcumin\ amount}{theoretical\ loaded\ curcumin\ amount} \times 100 \qquad (3)$$

2.2.3. Particle size distribution

Particle size distribution was determined after dispersion of each sample in deionized water at 0.1 mg/mL and sonication for 1 min. Measurements were conducted using the NanoSight NS300 (Malvern Panalytical, Grovewood Rd, United Kingdom), exploiting the Nanoparticle Tracking Analysis (NTA) technology. Each batch was analyzed three times (five captures of 90 s each). To assess the long-term stability of the prepared formulations, particle size analysis was repeated after 28 months of storage of the freeze-dried samples in a sealed glass vial at room temperature.

2.2.4. Scanning electron microscopy (SEM) and transmission electron microscopy (TEM)

SEM was performed using a high-resolution MIRA3 instrument (Tescan, Brno, Czech Republic) to assess the morphology. Briefly, samples were first observed as dried powder previously gold-sputter-coated under argon. Then, samples were dispersed in water to dissolve the mannitol; a drop of the sample was placed on a glass slide and left dry before being gold-sputter-coated under argon. The samples were imaged at 8 kV using an In-Beam SE detector, and the micro-analytical composition of samples was determined by Energy Dispersive X-ray Spectroscopy (EDS, EDAX) operating at 20 kV.

Moreover, a drop of the sample suspension (concentration = 0.1 mg/mL) was placed onto a 300-mesh nickel grid coated with carbon and observed by TEM (JEOL JEM 1200 EX working at 85 kV) to assess the morphology of SFNs-Fe compared to SFNs-CUR and Fe_2O_3 nanopowder. Before the measurement, the samples were dried for 24 h at room temperature (25 °C).

Field Emission Scanning Electron Microscopy (GeminiSEM-360, Carl Zeiss S.p.A, Milan, Italy) was used to assess the morphology of the nanosystems obtained via microfluidic. Samples were observed as dried powders previously Pt-sputter-coated (4 nm thick Pt layer) under argon (Emitech K575X Turbo Pumped Sputter Coater, Quorum Technologies, UK). The samples were imaged at an acceleration voltage of 5 kV using the InLens SE detector and working distances (WD) between 3.0 and 4.3 mm.

2.2.5. Fourier transform infrared (FT-IR) spectroscopy

IR spectra (650–4000 cm^{-1}) of lyophilized samples were recorded in ATR (attenuated total reflectance) using a Bruker Equinox 55 spectrometer equipped with a pyroelectric detector (DTGS type) with a 4 cm^{-1} resolution. The spectrometer runs Opus 7.8 software.

2.2.6. Thermogravimetric analysis (TGA)

The thermal behavior of all the freeze-dried SFNs was evaluated by TGA. The analyses were carried out in the 30–800 °C temperature range at a heating rate of 10 °C/min and N_2 stream of 20 mL/min (TGA 4000 Perkin Elmer, Milan, Italy) on exactly weighed amount of each sample. The residue water content of all SFNs was determined as the weight loss up to 125 °C, while the degradation behavior and the residual weight of each analyzed sample were compared up to 800 °C.

2.2.7. In vitro drug release test

For each batch, SFNs were suspended in deionized water, transferred into a dialysis membrane (3–5 kDa MWCO), immersed in 50 % *v/v* of ethanol in water, and maintained under mild magnetic stirring at 37 °C for 3 days. A precise volume of the release fluid was removed after predefined time intervals, analyzed spectrophotometrically, and replaced with fresh fluid to ensure sink conditions. The cumulative drug release % was calculated referring to the amount of drug loaded in the nanoparticles. The results are the average of three replicates.

2.2.8. Drug release kinetic study

The mechanism and kinetics of the drug release were defined, fitting the in vitro drug release data with different kinetic models.

⊞ Higuchi

$$F(t) = k \times t^{0.5} \qquad (4)$$

$$F(t) = 100 \times \left(1 - C \times exp.^{(-k \times t)}\right) \qquad (5)$$

where F(t) is the amount of drug released at time t, and *k* is the release constant. Eq. (5) is Eq. (2).12 from [39].

⊞ Peppas-Sahlin

$$F(t) = k_1 \times t^m + k_2 \times t^{(2 \times m)} \qquad (6)$$

where F(t) is the amount of drug released at time t, k_1 and k_2 are, respectively, the diffusion and erosion constant, and *m* is the diffusional exponent indicative of the drug release mechanism.

⊞ Ritger-Peppas

$$F(t) = k \times t^n \qquad (7)$$

where F(t) is the amount of drug released at time t, *k* is the release constant, and *n* is the release exponent indicative of the drug release mechanism.

⊞ Zero-order

$$F(t) = k \times t \qquad (8)$$

where F(t) is the amount of drug released at time t, and *k* is the release constant.

⊞ Korsmeyer-Peppas

$$F(t) = k_{KP} \times t^n \times Q_0 \qquad (9)$$

where F(t) is the amount of drug released at time t, k_{KP} is the release constant, *n* is the release exponent indicative of the drug release mechanism, and Q_0 is the initial amount of drug.

2.3. In vitro cellular assays

2.3.1. Cytocompatibility assay

The cytocompatibility was assessed according to the MTT test described by Orlandi et al. [38] after culturing mesenchymal stem cells (MSCs) seeded in a 96-well plate (10,000 cells/cm^2) with Dulbecco's

modified Eagle medium (DMEM) F12, 10 % *v/v* FBS, 1 % *v/v* penicillin/streptomycin, and 1 % *v/v* amphotericin B for 72 h. 100 μL of samples suspended in a culture medium (not supplemented with FBS) at the final concentrations of 0.08, 0.04, 0.02, and 0.01 mg/mL were added to cells, and after 24, 48, and 72 h of incubation, the supernatants were discarded, the cells were washed with PBS and analyzed. Untreated cells were considered as a control (100 % of metabolic activity).

2.3.2. Cellular uptake

MSCs were cultured at 37 °C and 5 % CO_2 as described above after being seeded in 96-well plates at a 5000 cells/cm^2 density. After 24 h, samples were added to each well at 0.02 and 0.04 mg/mL. After 30, 60, or 120 min, cells were washed with PBS, and curcumin fluorescence intensity was measured at 485 nm excitation and 528 nm emission, gain 90, using a microplate reader (Synergy HT, BioTek, UK). Cells not treated with samples were considered as controls. All experiments were performed in triplicate.

2.4. In vivo preliminary biodistribution studies

The animal experiments were carried out following the approved protocol and in line with the recommendation received from the Institutional Animal Care and Use Committee (Organismo Per il Benessere Animale, IRCCS Ospedale Policlinico San Martino of Genoa, Italy) and the National Istituto Superiore di Sanità. The studies were on 8-week-old C57bl/6 J mice using formulation D, considering the maximum tolerated SFN dose as 20–75 mg/kg [10,40–42] and an iron dose suitable for MRI in rodents up to 100 mg Fe/kg [43–46]. Mice were injected intramuscularly or subcutaneously into the flank with SFNs-Fe (50 mg/kg of SFNs in 200 μL of PBS, corresponding to 5 mg Fe/kg) and sacrificed after 24 h. In vivo MR imaging was performed before the SFNs injection, and after 2 and 24 h, animals were anesthetized by 4 % isofluorane inhalation in oxygen (1–1.5 % isofluorane for maintenance) and placed in a 7 T MRI system (Bruker Pharmascan) on a heated bed. T2* weighted images were acquired using a gradient-echo sequence with TR = 1158 ms, TE 4 ms, flip angle = 50°, matrix size = 256 × 256, FOV = 40 × 40 mm^2, 30 slices, and slice thickness = 0.8 mm.

2.5. Histological analysis

Morphological evaluation of the localization of SFNs-Fe was performed 24 h after subcutaneous or intramuscular inoculation in 2 C57bl/6 J mice. Hematoxylin and Eosin (H&E) and Perls' Prussian blue, which colors the iron particles blue, were used for the evaluation. Liver, splenic, kidney, heart, and lung tissues, lymph nodes, and muscles were fixed in 10 % formalin buffer, dehydrated, embedded in paraffin, and sectioned at 4 μm thickness. Tissue sections were stained with H&E for morphological examination and Perl's Prussian blue for iron accumulation according to standard protocols [47,48]. The procedure involves treating tissue sections with acidic ferrocyanide solutions: ferric ions (+3) in the tumor tissue react with ferrocyanide, producing a vivid blue pigment known as Prussian blue. Briefly, tissue sections were deparaffinized, hydrated in distilled water, and then immersed in a freshly prepared 1:1 mixture of hydrochloric acid (20 %) and potassium ferrocyanide solution (10 %). The tissue sections were then washed three times with distilled water and counterstained with nuclear-fast red for 5 min. Finally, the sections were observed under an optical microscope after rinsing with distilled water and 100 % alcohol, followed by xylene.

2.6. Microfluidic GMP-like production of nanoparticles

SFNs were prepared by nanoprecipitation in a glass capillary microfluidics device (Sunshine equipment, Unchained Labs, 4747 Willow Rd Pleasanton, CA 94588). The instrument has a total flow rate range of 0.1 to 30 mL/min, with a flow rate ratio (aqueous to organic) between 1:1 and 10:1, depending on the Chip used. It handles sample

Table 2
Y%, curcumin loading (D%), and EE% for each formulation. Mean values ± standard deviations were obtained by analyzing three batches per formulation.

Formulation	Y%	D%	EE%
SFNs-CUR	57.37 ± 1.86	18.97 ± 2.21	72.97 ± 8.48
A	63.43 ± 4.17	20.94 ± 0.19	80.56 ± 0.74
B	64.10 ± 9.29	23.14 ± 0.45	89.00 ± 1.74
C	57.01 ± 5.01	18.97 ± 2.52	72.98 ± 9.71
D	63.43 ± 8.34	19.29 ± 2.84	74.21 ± 10.93

volumes from 1 to 6.5 mL at a 3:1 flow rate ratio, with a minimum input of 320 μL, and supports continuous mode volumes from 20 mL to ∞. A GMP version is available for large-scale production, and since both lab and GMP instruments use the same mixing process and protocol, formulations can be seamlessly transferred to GMP production without adjustments. During the nanoprecipitation method, fibroin solution (1.5 % *w/v*) and acetone were pumped into the microfluidic device with a constant flow rate (1.5 mL/min). The SFNs synthesis process was optimized through variation in the geometry of the microfluidic device (micromixer Chip, part n. 3200401 or 5-input Chip, part n. 3200735) and the flow rate ratio (FRR), that is the volumetric ratio of the aqueous (fibroin) to the organic phase (acetone), which was set to 1:5, 1:4, 1:3, 1:2, and 1:1. Once prepared, samples were analyzed freshly to determine the particle size (as reported in Section 2.2.3) and, after freeze-drying (see Section 2.2.1), to evaluate the morphology by FESEM (see Section 2.2.4).

2.7. Statistical analysis

A linear generalized analysis of variance (ANOVA) model was applied to analyze the data with a normal distribution, and the differences between the groups were evaluated using Fisher's least significant difference (LSD) procedure (STATGRAPHICS XVII, Statpoint Technologies, Inc., Warrenton, Virginia, USA). In detail, when analyzing the data regarding the Y%, EE%, mean diameter, mode, d_{10}, d_{50} and d_{90}, the formulation was considered a fixed factor, while for the release data, even the time was considered a fixed factor. The kinetic models of release data were elaborated with Graph-Pad Prism software version 8.0.1. Cell metabolic activity data were first analyzed by considering the encapsulation of curcumin into the nanoparticles and the concentration of curcumin fixed factors; then, the analysis was repeated by considering the formulation, the time, and the concentration of nanoparticle fixed factors. The statistical significance was set at $p < 0.05$.

3. Results

SFNs-Fe nanoparticles were prepared using a desolvation method in acetone; the yield and the EE% for each formulation are summarized in Table 2. In detail, the Y% was consistently above 50 % for all the batches prepared without any significant difference ($p = 0.58$). The curcumin loading ranged from 18.97 % to 23.14 %, with an encapsulation efficiency above 70 % that was not affected by the increasing amounts of Fe_2O_3 added.

A complete characterization was then conducted to assess that the combined materials, i.e., SF and Fe_2O_3, are homogeneously distributed within the final SFNs-Fe formulations (Fig. 1). At first, the particle size distribution was investigated (Fig. 1A). The mean diameter of SFNs-Fe formulations is significantly larger than that of Fe_2O_3 nanopowder. In detail, following the decrease in the amount of Fe_2O_3 with respect to SF, an increase in the mean diameter was observed: from 131.0 nm for formulation D to 197.6 nm for formulation B. However, formulation A, with the lowest amount of Fe_2O_3, had a mean diameter of 129.1, significantly lower than formulation B. A similar trend was also observed for the d_{50} value: an increase was observed when lowering the amount of Fe_2O_3 incorporated, except for formulation A, for which the
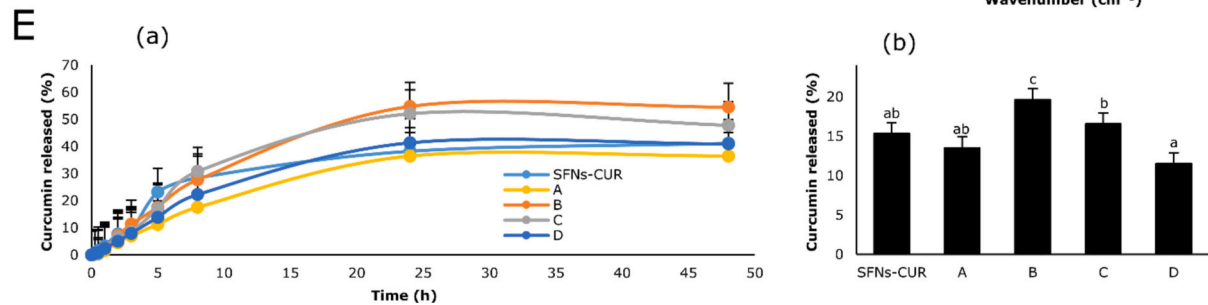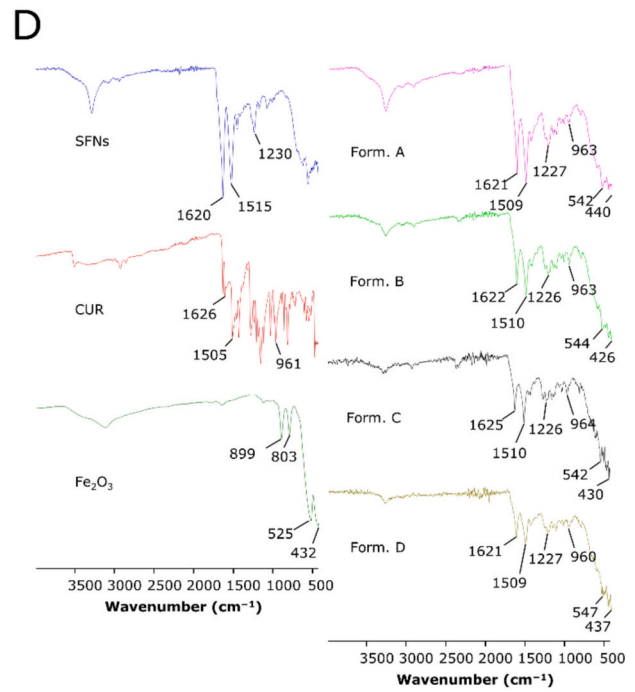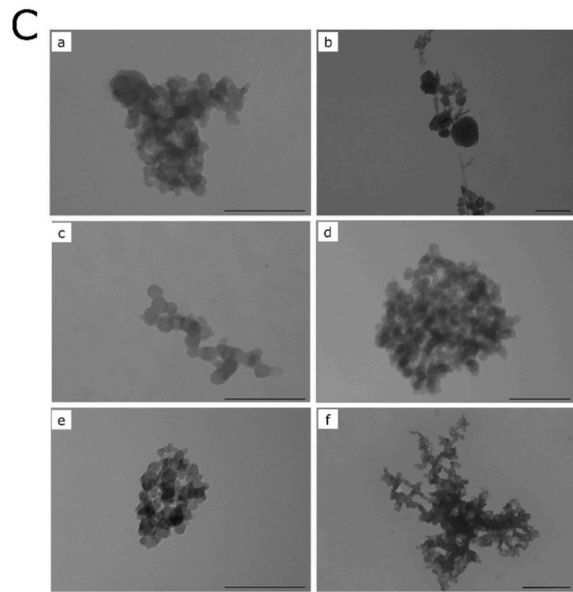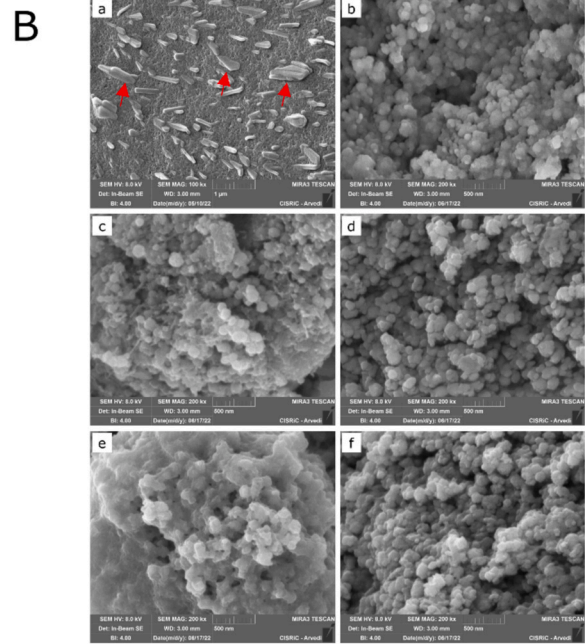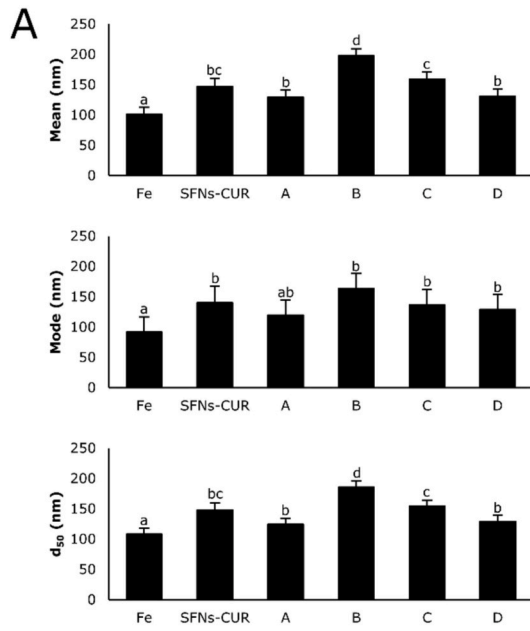
(caption on next page)

Fig. 1. Characterization of the prepared formulations. (A) Mean diameter, mode, and d_{50} of all the formulations compared with Fe_2O_3 nanopowder (Fe). Data are reported in nm as mean value $\pm$ LSD, Multifactor ANOVA, $n = 3$ independent measurements for each batch (five captures of 90 s each). Letters (a, b, ab, bc, c, and d) are used to compare the means of different groups. If the letters are different, there is a statistically significant difference between the means ($p < 0.05$); if the letters are the same, there is no statistically significant difference between the means ($p > 0.05$). (B) Representative SEM images of SFNs-CUR (a, b) and formulations A (c), B (d), C (e), and D (f). Magnifications: 100 k $\times$ (a) and 200 k $\times$ (b-f). Scale bars: 1 μm (a) and 500 nm (b-f). The red arrows indicate crystallized mannitol used as a cryoprotectant. (C) Representative TEM images of SFNs-CUR (a), Fe nanopowder (b), and SFNs-Fe formulations (c-f). Scale bar: 50 nm (b), 200 nm (a, c, d, e) and 500 nm (f). (D) FT-IR spectra of fibroin nanoparticles (SFNs), curcumin (CUR), Fe nanopowder (Fe_2O_3), and SFNs-Fe formulations. (E) In vitro drug release profiles of samples (a). Data are reported as the mean value of cumulative drug release percentage with respect to the amount of drug loaded in the nanoparticles. The grand mean of the amount of curcumin released (b). Data are reported as cumulative drug release percentage (mean value $\pm$ LSD, Multifactor ANOVA, $n = 3$ independent experiments). Letters (a, ab, b, and c) are used to compare the means of different groups. If the letters are different, there is a statistically significant difference between the means ($p < 0.05$); if the letters are the same, there is no statistically significant difference between the means ($p > 0.05$). (For interpretation of the references to colour in this figure legend, the reader is referred to the web version of this article.)

Table 3

Analytical composition of the formulations prepared. The analysis was conducted using images representative of the formulation.

Formulation	Element (% *w/w*)				
	C	N	O	S	Fe
SFNs-CUR	57.89	13.56	30.26	0.53	–
A	56.55	12.91	29.58	0.41	0.55
B	57.54	11.73	27.99	0.43	2.31
C	56.03	11.00	26.28	0.38	6.30
D	52.43	8.72	23.70	0.37	14.77

d_{50} value decreased. All the formulations showed a non-monomodal distribution, even if the mode was not significantly different among SFNs-Fe samples. After 28 months of storage at room temperature, the freeze-dried samples showed a significant reduction in mean diameter, mode, d_{10}, d_{50}, and d_{90} for some formulations compared to freshly prepared samples. This reduction is likely due to alterations in the nanoparticle surface during storage, which may have weakened adhesive forces, ultimately leading to reduced particle aggregation [49]. Still, the size of nanoparticles increased as the amount of incorporated Fe_2O_3 decreased, except in formulation A, which had the lowest Fe_2O_3 content and exhibited a decrease in size (see supplementary material, Fig. S1).

Representative SEM images of the samples were collected and are pictured in Fig. 1B. At lower magnification, it is possible to distinguish the crystallized mannitol for all the formulations (Fig. 1B, a; red arrows). Upon increasing magnification, nanoparticles in all formulations appeared as clusters rather than being uniformly dispersed, which is the consequence of the dispersing solvent evaporation during the sample preparation [50–53]. However, the individual particles in all formulations displayed globular structures with a spherical shape and a particle size below 200 nm (Fig. 1B, b-f). All the samples appeared homogenous and uniform, without significant morphological differences among the prepared batches and formulations.

Energy Dispersive X-ray Analysis was used to evaluate the microanalytical composition of samples (Fig. S2 in the supplementary material and Table 3). Carbon (C), Nitrogen (N), Oxygen (O), and Sulfur (S) were the main components of the samples, related to the presence of SF, which is a protein. Regarding the amount of Fe present in SFNs-Fe, as expected, it was more abundantly present in formulation D (that has the highest Fe_2O_3 amount; see Table 1) and decreased when the amount of incorporated Fe_2O_3 was reduced. Furthermore, consistency between theoretical and actual loading of Fe was observed, as for all the formulations, the Fe element % was about double of Fe_2O_3 (indeed, 1 mol of Fe_2O_3 contains 2 mol of Fe). However, this was true apart for the formulations with the lowest Fe_2O_3 amount, likely because this is a quali-quantitative analysis.

To further confirm the uniformity and to investigate the morphology of SFNs-Fe deeply, TEM images were acquired (Fig. 1C). Fe_2O_3 nanopowder appeared irregular, with some spherical particles mixed with long sticks (Fig. 1C, b). Such non-homogeneity disappeared in SFNs-Fe samples (Fig. 1C, c-f), which showed a morphology similar to SFNs-CUR (Fig. 1C, a) and appeared mainly aggregated. No significant

morphological differences among the prepared batches and formulations were observed, even in this case. Importantly, it was impossible to distinguish Fe from SF, suggesting a homogeneous distribution of the two components.

The IR spectrum of SFNs showed characteristic peaks of amide A (3280 cm^{-1}, νN-H), amide I (at about 1621 cm^{-1}, νC=O), amide II (at about 1515 cm^{-1}, δN-H + νC-N), and amide III (at about 1230 cm^{-1}, νC-N + δN-H) (Fig. 1D, SFNs). Typical absorption bands of curcumin appeared in the 3500–3200 cm^{-1} range, due to νO-H, at 1626 cm^{-1} (νC=O), 1505 cm^{-1} (νC=O + δCCC + δCC=O), and at 962 cm^{-1} (cis-trans C—H vibration of the aromatic ring) (Fig. 1D, CUR). A strong band below 700 cm^{-1} is assigned Fe—O lattice vibrations [54]; in detail, the bands corresponding to the Fe—O stretching mode of Fe_2O_3 are seen at 525 and 432 cm^{-1} in Fe nanopowder (Fig. 1D, Fe_2O_3); signal at 899 cm^{-1} can be attributed to Fe-O-H bending vibrations. All SFNs-Fe showed the characteristic bands of fibroin and curcumin, with the bands corresponding to Fe_2O_3 seen at 540 and 432 cm^{-1}; the shift of Fe_2O_3 bands towards higher values suggests the interaction between fibroin and Fe nanopowder. As expected, the characteristic bands of Fe_2O_3 were more resolved in SFNs-Fe prepared with higher amounts of Fe_2O_3.

TGA curves and their corresponding derivative functions (DTGA) (not shown) of the sample of each formulation showed a similar trend, indicating that the presence of Fe_2O_3 in the SNFs did not influence their degradation behavior. The thermal curves of all formulations revealed a two-step degradation profile: an initial weight loss in the 30–125 °C temperature range and the other at temperatures above about 200 °C. The first step is attributable to the loss of moisture: the residue water content of all SFNs, equal to 5.6 $\pm$ 0.7 %, did not vary with the concentration ratio of Fe_2O_3 and confirmed the efficacy of the freeze-drying process in drying and removing (free and bonded) water [55,56]. The second step is due to the decomposition and degradation of the organic material of the analyzed sample, i.e., fibroin and curcumin [38]: all the thermal curves were almost superimposable, indicating that, as with the water content, the degradation behavior of SFNs was not affected by the presence of Fe_2O_3. Last, as expected, the residual weight of the sample of formulation A was significantly different from that of SFNs-CUR (about 36 % vs. 29 %, respectively): this can be ascribable to the higher amounts of Fe_2O_3, corresponding to the inorganic non-combustible fraction of the nanoparticles.

All the samples showed a similar release profile, with time having a significant effect ($p < 0.001$): a release between 17 and 31 % was observed up to 8 h, followed by reaching a plateau after 24 h (Fig. 1E, a). However, the formulation influenced the amount of curcumin released and the release rate ($p < 0.0001$). For example, it can be observed that formulation D releases the lowest amount of curcumin most slowly. At the same time, B is the formulation that releases the most and the fastest. To better highlight this aspect, the grand mean resulting from the statistical analysis of the release data has been reported in Fig. 1E, b. As can be seen, formulation B was the one that released a significantly highest amount of curcumin, followed by formulation C, then D, and finally A, which released a curcumin amount that was not significantly different from that of SFNs-CUR. Therefore, decreasing the amount of

Table 4
Results of in vitro release model fitting for all the formulations. Kinetic elaborations were performed on the release data from at least three independent experiments for each batch.

Model	Equation	Formulation	Coefficients (95 % confidence bounds)	Sum of squares	R^2	Degrees of freedom
Higuchi	$F(t) = k \times t^{0.5}$	SFNs-CUR	k = 0.07262 (0.06337, 0.08187)	0.05996	0.8680	17
		A	k = 0.0999 (0.08531, 0.1145)	0.0712	0.8786	17
		B	k = 0.1549 (0.1256, 0.1842)	0.2868	0.8115	17
		C	k = 0.14 (0.1203, 0.1598)	0.1305	0.8849	17
		D	k = 0.1103 (0.09497, 0.1257)	0.07897	0.8864	17
Higuchi (eq. 2.12 from [39])	$F(t) = 100 \times (1\text{-}C \times \exp.^{(-k \times t)})$	SFNs-CUR	C = 0.9991 (0.9986, 0.9997) k = 0.0000883 (0.00005745, 0.0001191)	0.1369	0.6986	16
		A	C = 0.9998 (0.9995, 1.000) k = 0.0002423 (0.0002065, 0.0002781)	0.04213	0.9282	16
		B	C = 0.9996 (0.9989, 1.000) k = 0.0003728 (0.0002877, 0.0004581)	0.2375	0.8439	16
		C	C = 0.9996 (0.9992, 1.000) k = 0.000336 (0.0002839, 0.0003882)	0.08911	0.9214	16
		D	C = 0.9997 (0.9993, 1.000) k = 0.000263 (0.0002223, 0.0003037)	0.0545	0.9216	16
Peppas-Sahlin	$F(t) = k_1 \times t^m + k_2 \times t^{(2 \times m)}$	SFNs-CUR	k_1 = −1.057 (−∞, −0.2080) k_2 = 1.121 (−0.006050, +∞) m = 0.0618 (−0.001106, 0.1449)	0.03177	0.9301	15
		A	k_1 = −0.1719 (−0.2990, −0.01893) k_2 = 0.2297 (0.1599, 0.3629) m = 0.2094 (0.06890, 0.4052)	0.01827	0.9606	15
		B	k_1 = −0.3171 (−1.426, 0.1252) k_2 = 0.222 (0.09688, 2.372) m = 0.371 (−0.004253, 1.478)	0.1624	0.8933	15
		C	k_1 = −0.2649 (−0.6028, −0.04588) k_2 = 0.2273 (0.1568, 0.3314) m = 0.3158 (0.1156, 0.6467)	0.03289	0.971	15
		D	k_1 = −0.1818 (−0.4448 to −0.0188) k_2 = 0.2367 (0.1611 to 0.3558) m = 0.2246 (0.07098, 0.4814)	0.02199	0.9684	15
Ritger-Peppas	$F(t) = k \times t^n$	SFNs-CUR	k = 0.08513 (0.05740, 0.1160) n = 0.4495 (0.3514, 0.5648)	0.05658	0.8755	16
		A	k = 0.0534 (0.03757, 0.07145) n = 0.7505 (0.6469, 0.8700)	0.02423	0.9587	16
		B	k = 0.08673 (0.04501, 0.1390) n = 0.7329 (0.5609, 0.9528)	0.1851	0.8784	16

Table 4 (*continued*)

Model	Equation	Formulation	Coefficients (95 % confidence bounds)	Sum of squares	R^2	Degrees of freedom
		C	k = 0.07831 (0.05547, 0.1042) n = 0.7331 (0.6309, 0.8507)	0.0485	0.9572	16
		D	k = 0.06223 (0.04419, 0.08269) n = 0.7298 (0.6280, 0.8466)	0.02979	0.9572	16
Zero-order	F(t) = k × t	SFNs-CUR	k = 0.01153 (0.008322, 0.01474)	0.2345	0.4838	17
		A	k = 0.02567 (0.02259, 0.02875)	0.04922	0.9161	17
		B	k = 0.0396 (0.03256, 0.04664)	0.2571	0.831	17
		C	k = 0.03579 (0.03127, 0.04031)	0.1061	0.9064	17
		D	k = 0.02817 (0.02459, 0.03174)	0.06634	0.9046	17
Korsmeyer-Peppas	F(t) = k_{KP} × t^n × Q_0	SFNs-CUR	k_{KP} = 0.08513 (0.05740, 0.1160) n = 0.4495 (0.3514, 0.5648)	0.05658	0.8755	16
		A	k_{KP} = 0.0534 (0.03757, 0.07145) n = 0.7505 (0.6469, 0.8700)	0.02423	0.9587	16
		B	k_{KP} = 0.08673 (0.04501, 0.1390) n = 0.7329 (0.5609, 0.9528)	0.1851	0.8784	16
		C	k_{KP} = 0.07831 (0.05547, 0.1042) n = 0.7331 (0.6309, 0.8507)	0.0485	0.9572	16
		D	k_{KP} = 0.06223 (0.04419, 0.08269) n = 0.7298 (0.6280, 0.8466)	0.02979	0.9572	16

incorporated Fe_2O_3 leads to an increased curcumin release, except for formulation A (with the lowest amount of Fe), for which a decrease was observed.

The effect of Fe on the release mechanism of curcumin from SFNs-Fe samples was further highlighted by elaborating the release data with the commonly employed kinetic models (Table 4). All samples adequately fitted with the models, with some exceptions (SFNs-CUR for Eq. (5), R^2 = 0.6986; SFNs-CUR for Eq. (8), R^2 = 0.4838). Therefore, theoretically, the release of curcumin from the SF matrix can occur by diffusion through the material's porosity or following case-II relaxation. Regarding diffusion, the *n* exponent calculated from the Ritger-Peppas and Korsmeyer-Peppas equations was between 0.43 and 0.85 for all the formulations, indicating an anomalous (non-Fickian) transport [57,58]. However, diffusion is not the only mechanism; case-II relaxation also has a role. Confirmation of this comes from the Peppas-Shalin model, where both the Fickian contribution (first term of the equation, *k1*) and the case-II relaxation contribution (second term of the equation, *k2*) are considered [59]: as *k2* > *k1*, and the *k1* value is negative, the case-II relaxation is predominant on the diffusion phenomenon (even if not exclusive) in the release of curcumin. Accordingly, the coefficient *m* of the Peppas-Shalin model (which relates to the purely Fickian diffusion exponent) is different from the *n* value calculated with the Peppas-Shalin equation, further confirming that the release mechanism of curcumin from SFNs also depends on case II relaxation [60]. The addition of Fe_2O_3, especially the added amount, affects the balance of these mechanisms. Looking at the Peppas-Shalin model, an increase in *k1* with respect to SFNs-CUR was observed when adding Fe; for SFNs-Fe formulations, the *k1* decreased when lowering the amount of Fe_2O_3 incorporated, except then increase again for formulation A, with the lowest amount of Fe_2O_3. The same effect was observed in the Higuchi

model (a good indicator in a diffusion-controlled drug delivery system). The increase in the diffusion phenomenon induced by Fe_2O_3 is associated with a decrease in the case-II relaxation, as the *k2* calculated from the Peppas-Shalin model decreased by adding Fe_2O_3 in the formulation with respect to SFNs-CUR.

Fig. 2 reports the results of in vitro testing for all the formulations. Encapsulation of curcumin into SFNs reduced the toxic effect (Fig. 2A, a). Indeed, cell metabolic activity decreased after increasing the concentration of free curcumin but not increasing the SFNs-CUR concentration, even when an equivalent amount of curcumin was reached. Furthermore, all the SFN formulations showed cytocompatibility, as the cell metabolic activity was above 80 % at all the tested concentrations (Fig. 2A, b-e). Specifically, the treatment time and formulation (and thus the amount of Fe_2O_3) do not significantly affect cell metabolic activity (p = 0.0807 and p = 0.108, respectively). Conversely, cell metabolic activity significantly increased by increasing the concentration of SFNs ($p < 0.05$).

The uptake of each formulation is reported in Fig. 2B. Preliminary analysis of cellular uptake data identified 72 h and 0.04 mg/mL as the optimal conditions to assess cellular uptake (Figs. 2B, a-b). Indeed, for these conditions, the uptake of all formulations by cells was the maximum. However, adding Fe_2O_3, especially the amount added, modifies the cellular uptake of SFNs-Fe (Fig. 2B, c). In detail, cellular uptake increased when the amount of added Fe_2O_3 was lowered, reaching the maximum for formulation B but then decreasing again for formulation A, which had the lowest amount of Fe_2O_3.

Fig. 3 reports MR images following the administration of formulation D to mice. The presence of magnetic cores within tissues reduces the relaxation times of the protons in the surrounding water, resulting in a darkening effect in those areas on MR imaging. Specifically, it was
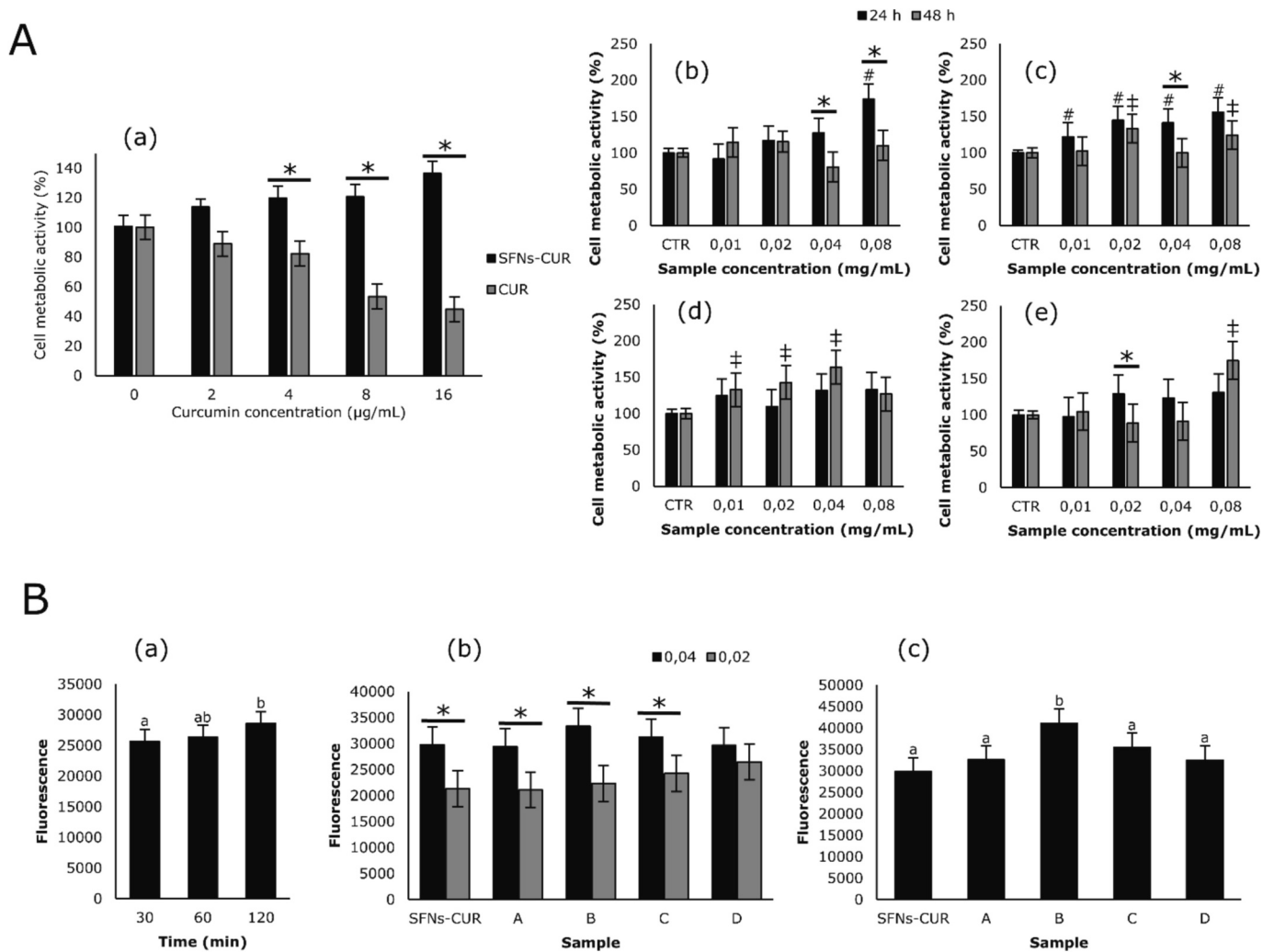
Fig. 2. (A) Percent cell metabolic activity of MSCs treated with SFNs-CUR and the equivalent amount of free curcumin (a) after 24 h, and with increasing concentrations of formulation A (b), B (c), C (d), and D (e) for 24 and 48 h. Cells not treated with samples were considered as a control (CTR = 100 % metabolic activity). Data are reported as mean value ± LSD, Multifactor ANOVA, $n = 3$ independent experiments. * Indicates a significant difference between the groups ($p < 0.05$). # and ‡ indicate a significative difference ($p < 0.05$) vs CTR 24 h and CTR 48 h, respectively. (B) Effect of incubation time (a) and nanoparticle concentration (b) on cellular uptake. Cellular uptake of formulations after incubation at 0.04 mg/mL for 72 h (c). Data are reported as mean value ± LSD, Multifactor ANOVA, n = 3 independent experiments. Letters (a, ab, and b) are used to compare the means of different groups. If the letters are different, there is a statistically significant difference between the means ($p < 0.05$); if the letters are the same, there is no statistically significant difference between the means ($p > 0.05$). * Indicates a significant difference ($p < 0.05$) between the two groups.

shown that subcutaneous (Fig. 3A) and intramuscular (Fig. 3B) injection of SFNs-Fe into the back of the mice caused darkening at those injected anatomical locations in MR images; that darkening was visible as long as 24 h post intramuscular injection (Fig. 3B).

Iron accumulation in tissues was examined after subcutaneous injection of formulation D: a minimal presence of iron was observed in Kupffer cells at the level of liver sinusoids in the absence of hepatocellular accumulation, and slight iron accumulation was observed in marginal sinus histiocytes in the context of isolated lymph nodes. Occasional very rare iron-containing macrophages have been observed in skeletal perimuscular adipose tissue next to the injection site (Fig. 4A). No accumulation of iron was observed in either kidney, heart, or lung tissues (data not shown). Regarding spleen iron accumulation, we compared Perls' staining images from a C57bl/6 J mouse subcutaneous injected with formulation D with those of a C57bl/6 J control mouse, as it is known that iron accumulates typically in the spleen [61]. We found a moderate accumulation of iron mainly in macrophages in the context of the red pulp with fewer Perls' positive macrophagic elements in the context of the white pulp in the injected mouse compared to the control mouse.

Finally, a GMP-compliant and scalable microfluidic technology has been used to optimize the preparation of SFNs. As can be seen in Fig. 5A, the particle size of SFNs is influenced both by the geometry of the microfluidic device (5-input Chip, T or micromixer, M) and the SF/acetone ratio. Overall, SFNs prepared with the microfluidic technology had a particle size lower than SFNs prepared manually (considered as CTR), with the mode consistently below 100 nm. Differences were observed among the SFNs prepared using the microfluidic procedure. In detail, the mean diameter was significantly lower for SFNs prepared with the micromixer device and using an SF/acetone ratio of 1:5. That mean size was not significantly different from the one of SFNs prepared with the 5-input Chip and using an SF/acetone ratio of 1:3. For the micromixer Chip, the particle size of SFNs increased when reducing the SF/acetone ratio from 1:5 to 1:3, and it was not possible to obtain nanoparticles with SF/acetone ratios of 1:2 and 1:1. A different trend was observed when using the 5-input Chip: the particle size decreased when decreasing the SF/acetone ratio from 1:5 to 1:3. In that case, it was still possible to obtain SFNs using the 1:2 SF/acetone ratio, and their
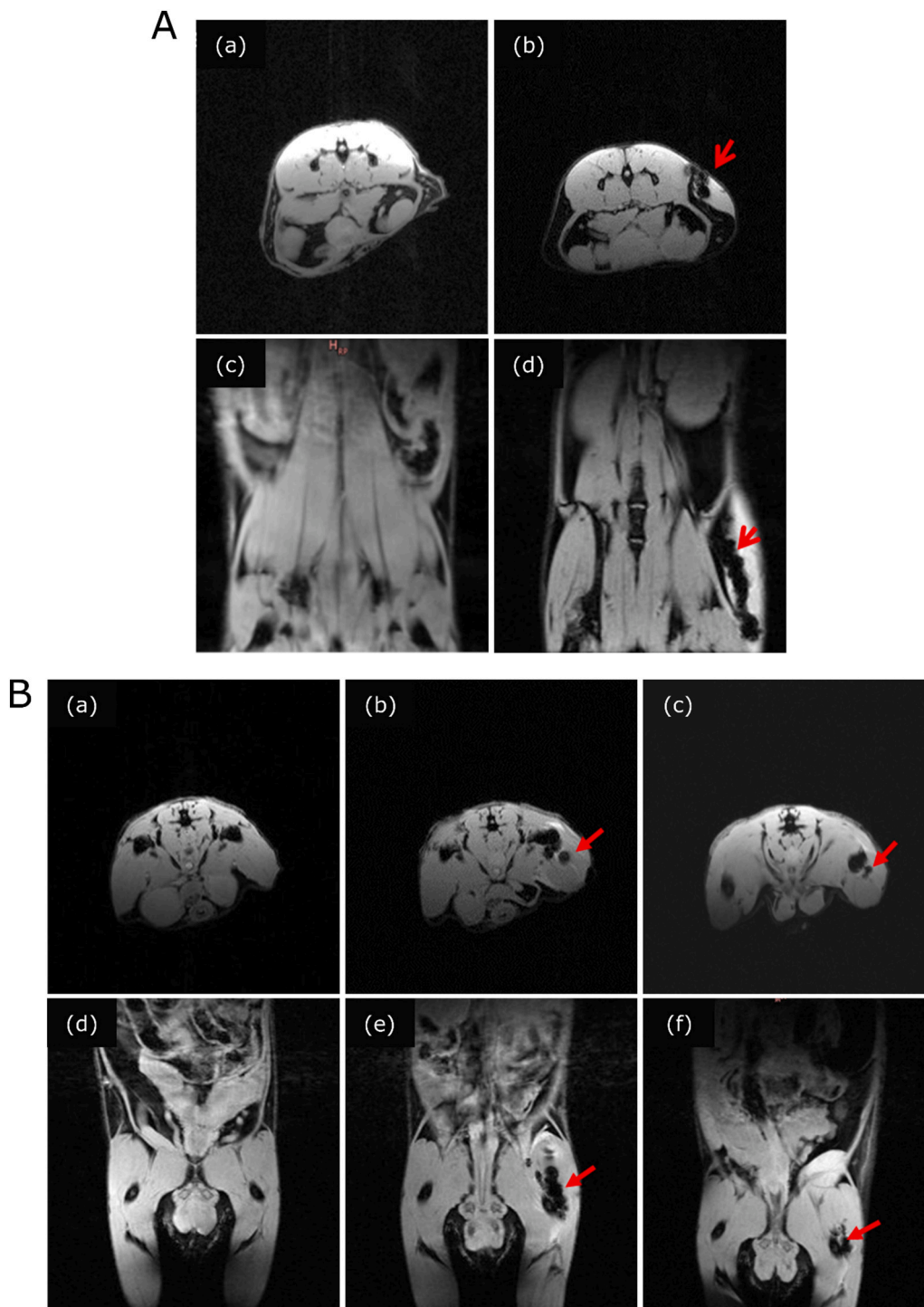
Fig. 3. (A) MR imaging before formulation D subcutaneous injection (a, c) and after 2 h (b, d). Axial (a, b) and coronal view (c, d). (B) MR imaging before formulation D intramuscular injection (a, d) and after 2 h (b, e) or 24 h (c, f). Axial (a, b, and c) and coronal view (d, e, and f).

particle size, despite being significantly higher with respect to one of the SFNs prepared with the micromixer Chip, was still smaller than the one of CTR. All the prepared samples exhibited a round shape morphology, as confirmed by FESEM imaging (Fig. 5B and Fig. S3 in the supplementary material). This indicates that nanoprecipitation occurs even with reduced acetone usage and also corroborates the size trend observed by NTA analysis. The transition of SF in β-sheet structures was also confirmed by FTIR analysis (data not shown).

4. Discussions

In this paper, SFNs loaded with curcumin were prepared using a desolvation method with acetone. To make these nanoparticles suitable for theranostic applications and biodistribution studies, increasing amounts of Fe_2O_3 were incorporated during the preparation process, obtaining five final SFNs-Fe formulations. Morphological analysis using SEM and TEM demonstrated a uniform distribution of the combined materials in the final SFNs-Fe formulations. Additionally, the microanalytical composition confirmed that the actual Fe loading matched
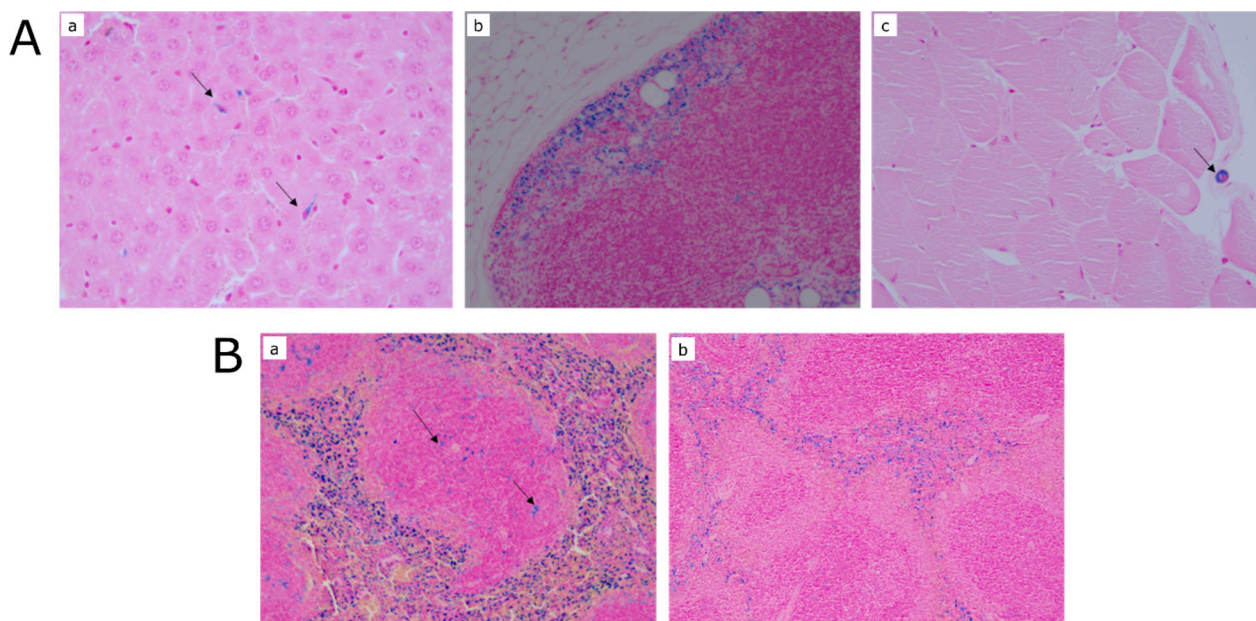
Fig. 4. Iron accumulation in the tissues. (A) Perls' staining of representative paraffin-embedded tissue sections from (a) the liver, (b) lymph node, and (c) perimuscolar adipose tissue of 8-week-old C57bl/6 J mice subcutaneously injected with formulation D. The blue stain represents iron accumulation. The arrows in (a) indicate iron accumulation in Kupffer cells at the level of the liver sinusoids, and the arrows in (c) indicate iron accumulation in macrophagic elements in the context of skeletal perimuscular adipose tissue. (B) Perls' staining of representative paraffin-embedded tissue sections from the spleen of 8-week-old C57bl/6 J mice subcutaneously injected with formulation D (a) and from the spleen of 8-week-old control C57bl/6 J mice. Leica DM 2000 microscope; A) Magnification 40× (a); 10× (b); 40× (c); B) Magnification 10× (a); 4× (b). (For interpretation of the references to colour in this figure legend, the reader is referred to the web version of this article.)

the theoretical predictions, and accordingly, the IR characterization revealed more distinct characteristic bands of Fe_2O_3 in SFNs-Fe formulations prepared with higher amounts of Fe_2O_3 (formulation D). Differently from what was reported in the literature, the SFNs-Fe prepared had a round-shape morphology where Fe_2O_3 was homogeneously dispersed in the SF matrix; thus, they differ from the nanoparticles prepared by Deng and colleagues, where a cubic core-shell structure was seen, with iron oxide nanoparticles coated with SF [37].

Interestingly, we also demonstrated, for the first time to the best of our knowledge, that the physical-chemical properties of the obtained SFNs-Fe varied based on the amount of incorporated Fe_2O_3. For example, both the mean diameter and the d_{50} value increased as the amount of incorporated Fe_2O_3 decreased, except in formulation A, which had the lowest Fe_2O_3 content and exhibited a decrease in size. A similar pattern was observed in curcumin release: reducing the Fe_2O_3 content led to increased curcumin release, except in formulation A, which showed a decrease despite having the least Fe_2O_3. This indicates that the precipitation of SF into SFNs during desolvation behaves differently depending on the Fe_2O_3 content. To better understand this, the effect of Fe on curcumin release mechanisms was further investigated using common kinetic models to analyze the release data. Considering that the release of curcumin from the SF matrix can occur by diffusion through the material's porosity or case-II relaxation, the addition of Fe_2O_3, especially the added amount, affects the balance of these mechanisms. In detail, it was revealed that adding Fe_2O_3 increases the curcumin released through diffusion, and it is likely that SF precipitation into nanoparticles following desolvation happens with different behaviors in dependence on the different amounts of Fe_2O_3, leading to an increased (or decreased) compactness of the polymer matrix. To the best of our knowledge, a similar effect has not yet been described in the literature. Our data suggest that a low (but not too low as for formulation A) amount of Fe_2O_3 induces more compactness of the fibroin matrix (thus hampering the diffusion of curcumin, which is indeed lowered), while a higher amount of Fe_2O_3 allows more diffusion due to reduced compactness of the fibroin matrix. As the compactness of

fibroin is higher, the mean diameter of SFNs-Fe with a low amount of Fe_2O_3 could be expected to be lower than the one of SFNs-Fe with a high amount of Fe_2O_3, but this is not the case (see Fig. 1A). Indeed, formulation B (low Fe_2O_3) has a higher diameter than formulation D (high Fe_2O_3). An explanation of this may come from the fact that the reduced compactness of the fibroin matrix may increase nanoparticle hydration, increasing the mean diameter measured by NTA that works with scattered light [62–64].

All the formulations showed cytocompatibility, and the encapsulation of curcumin into SFNs prevented its cytotoxic effect. The incorporation of iron oxide did not affect the cell metabolic activity, which, overall, significantly increased by enhancing the concentration of SFNs, likely as the consequence of the activation of cell metabolism to degrade the uptaken nanoparticles. Conversely, the amount of iron oxide incorporated in SFNs modified the in vitro uptake by cells. Indeed, even in this case, despite not being statistically significant, the same trend of the mean diameter, d_{50}, and amount of curcumin released was observed: the cellular uptake increased when the amount of incorporated Fe_2O_3 was lowered, except for formulation A, the one with the lowest amount of Fe_2O_3, for which it decreased again. It is likely that, even in this case, this is the consequence of the different behavior of SF in precipitating into SFNs as a function of the quantity of Fe_2O_3 incorporated in the mixture, which, as explained above, may have affected both the size and porosity. In this regard, it is well known from the literature that the size and porosity of nanoparticles may directly affect the mechanism of uptake and the in vivo deposition of protein corona on nanoparticles' surface, which in turn can affect, again, cell uptake [65]. Considering the cytocompatibility data in relation to the released curcumin, it may seem surprising that there is no cytotoxicity after 24 h, even though 30–40 % of the curcumin has been released from the nanoparticles by that time. This lack of cytotoxicity can be explained by considering the nanoparticle uptake and intracellular processing. As we demonstrated in this and previous studies, SFNs are efficiently internalized by various cell lines [13,17]. Within 30 min, uptake is nearly complete regardless of slight variations in experimental conditions such as cell line, culture
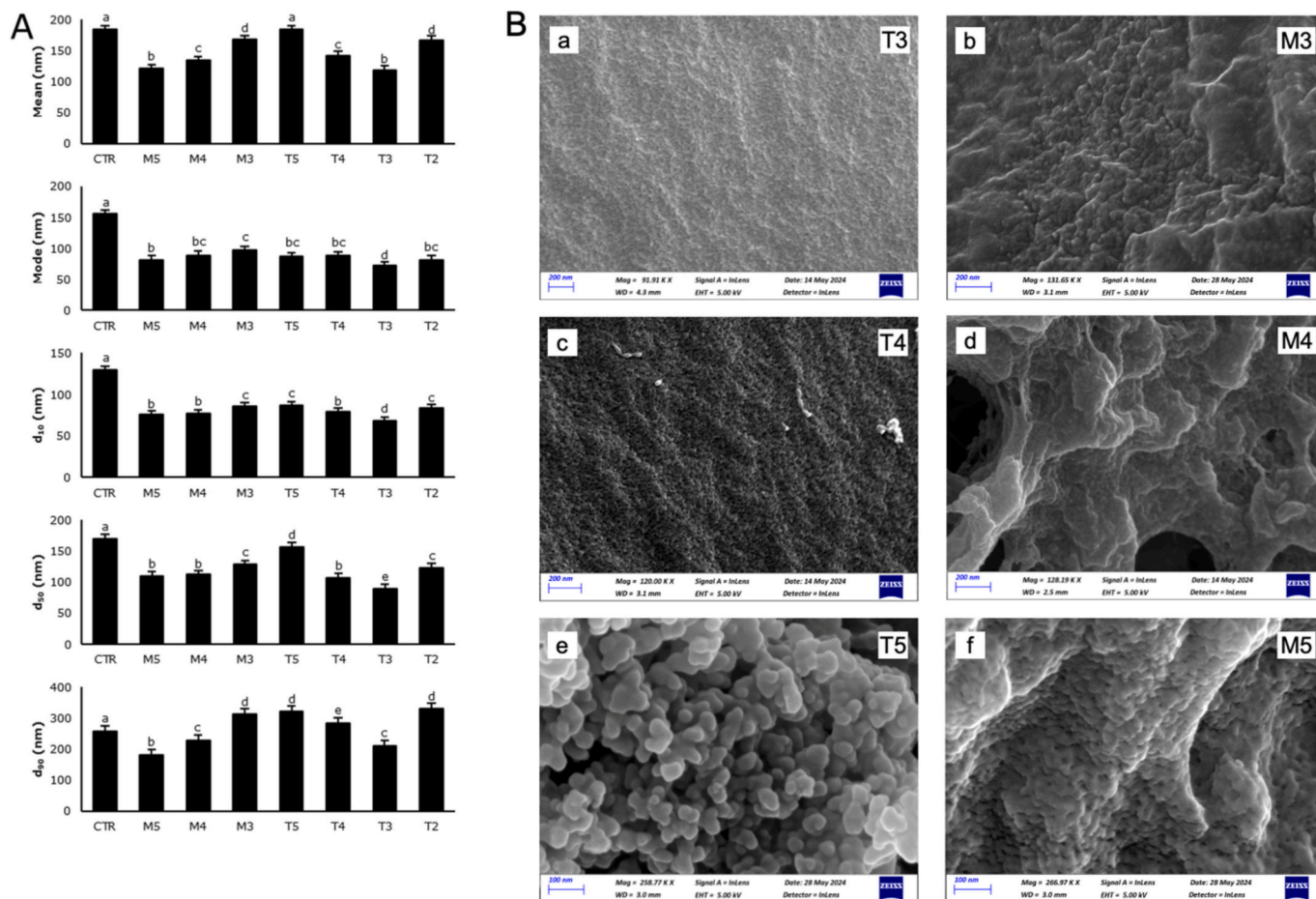
Fig. 5. GMP-compliant SFNs prepared by a microfluidic device. (A) Mean diameter, mode, and d_{50} of all the formulations compared with Fe_2O_3 nanopowder (Fe). Data are reported in nm as mean value $\pm$ LSD, Multifactor ANOVA, $n = 5$ independent measurements for each batch. Letters (a, b, bc, c, d, and e) are used to compare the means of different groups. If the letters are different, there is a statistically significant difference between the means ($p < 0.05$); if the letters are the same, there is no statistically significant difference between the means ($p > 0.05$). (B) Representative FESEM images of samples prepared by microfluidic.

media, or nanoparticle concentration. During this initial uptake period, the amount of curcumin released is minimal ($<2\%$ on average), which is insufficient to exert cytotoxic effects. Studies tracking the intracellular fate of SFNs [66–69] show that these nanoparticles are initially detected in the cytoplasm and then rapidly trafficked to endo- and lysosomal compartments. According to Florczak and colleagues [70], once in lysosomes, both the nanoparticles and their drug cargo are likely degraded, which mitigates the cytotoxicity of the released drug. Additionally, other potential mechanisms for drug cytotoxicity mitigation could include the elimination of nanoparticles through the release of exosomes [70].

Overall, the proposed desolvation method allowed homogeneous incorporation of Fe into the fibroin matrix, with minimal changes in the structure and properties, allowing the achievement of SFNs optimal for the biodistribution studies, which is also relevant in their clinical translation. Indeed, by MRI, we demonstrated that, following administration, most of the nanoparticles are retained at the administration site. Histological examination revealed only a moderate accumulation of iron in the spleen, mainly in the context of macrophages in the red pulp, as well as a slight iron accumulation in marginal sinus histiocytes in the context of isolated lymph nodes. No accumulation of iron was observed in either liver, kidney, heart, or lung tissues. These data are consistent with the reported evidence that particles in the range of 100 nm are more prone to entering interstitial lymphatic capillaries with respect to blood capillaries. In contrast, those that exceed 100 nm tend to remain at the injection site, supporting the use of SFNs for locoregional cancer therapy [71].

A noteworthy achievement of this work also lies in overcoming technical and economic challenges in SFN preparation using microfluidic technology. While the literature already reports the preparation of SFNs by microfluidic technology [72,73], demonstrating the feasibility to scale-up SFN production, to the best of our knowledge, this paper is the first to adopt a scalable and GMP-compliant microfluidic technology. As such, it represents a significant advance with respect to the literature, as it allows for the preparation of GMP SFNs at a scale suitable for clinical applications. As expected, the microfluidic approach proved advantageous in enabling precise control over particle size and uniformity, which are critical for the reproducibility and scalability of nanoparticle production. Indeed, the microfluidic technology enabled the production of consistently smaller particle sizes compared to manual methods, with the size influenced by the geometry of the device and the SF/acetone ratio. Still, it also allowed for the reduction of the amount of acetone needed to obtain nanoparticles, which is relevant from an environmental and economic point of view. Overall, achieving these technical and economic efficiencies makes SFNs competitive with nanoparticles formulated with other polymers, this being a considerable step forward for commercial translation; meanwhile, the possibility of obtaining GMP SFNs represents a considerable step forward for their application in the clinic.

5. Conclusions

We provide a straightforward desolvation method to create uniform SFNs incorporating varying amounts of Fe_2O_3 (SFNs-Fe), which are

detectable via MRI and loaded with curcumin as a model lipophilic drug. Morphological studies confirmed the uniform distribution of materials in the SFNs-Fe, and micro-analytical and IR characterization verified the consistency of Fe_2O_3 loading. The physical-chemical properties of SFNs-Fe varied with Fe_2O_3 content, affecting the compactness of the polymer matrix, and thus, the mean diameter (smaller with higher Fe_2O_3) and the drug release mechanism (more Fe_2O_3 led to greater curcumin release through diffusion). All formulations were cytocompatible, with curcumin encapsulation reducing its cytotoxicity and iron oxide not affecting cell metabolic activity, and easily uptaken by cells. SFNs-Fe were useful for preliminary biodistribution studies, as MRI confirmed significant retention at the administration site with only a slight to moderate iron accumulation in lymphoid tissues, i.e., lymph nodes and spleen, revealed by histological analysis, supporting their potential for localized cancer therapy. Finally, using microfluidic technology, SFNs with smaller sizes were produced compared to manual methods, with particle size influenced by device geometry and SF/acetone ratio. Being the microfluidic technology used GMP-compliant other than scalable, it represents a considerable step forward for SFN clinical and commercial translation.

Funding

CRediT authorship contribution statement

Francesca Ferrera: Writing – review & editing, Writing – original draft, Investigation, Data curation. **Roberta Resaz:** Writing – review & editing, Investigation. **Elia Bari:** Writing – review & editing, Writing – original draft, Supervision, Investigation, Funding acquisition, Conceptualization. **Daniela Fenoglio:** Writing – review & editing, Supervision, Investigation. **Luca Mastracci:** Writing – review & editing, Investigation. **Ivana Miletto:** Writing – review & editing, Investigation. **Angelo Modena:** Investigation. **Sara Perteghella:** Writing – review & editing, Investigation. **Marzio Sorlini:** Writing – review & editing, Project administration, Funding acquisition. **Lorena Segale:** Writing – review & editing, Supervision, Funding acquisition, Conceptualization. **Gilberto Filaci:** Writing – review & editing, Supervision, Conceptualization. **Maria Luisa Torre:** Writing – review & editing, Supervision, Project administration, Formal analysis, Conceptualization. **Lorella Giovannelli:** Writing – review & editing, Supervision, Investigation, Conceptualization.

Declaration of competing interest

Sara Perteghellaa and Maria Luisa Torre are co-founders and members of the company's advisory board Pharmaexceed S.r.l. Marzio Sorlini is the CEO of Pharmaexceed S.r.l. This company had no role in the design of the study, in the collection, analysis, or interpretation of data, in the writing of the manuscript, or in the decision to publish the results.

Acknowledgments

Appendix A. Supplementary data

Supplementary data to this article can be found online at https://doi.org/10.1016/j.ijbiomac.2024.137121.

Data availability

Data will be made available on request.

References

[1] W. Zhu, Z. Wei, C. Han, X. Weng, Nanomaterials as promising Theranostic tools in Nanomedicine and their applications in clinical disease diagnosis and treatment, Nanomaterials 11 (2021).

[2] L.D. Koh, Y. Cheng, C.P. Teng, Y.W. Khin, X.J. Loh, S.Y. Tee, M. Low, E.Y. Ye, H. D. Yu, Y.W. Zhang, M.Y. Han, Structures, mechanical properties and applications of silk fibroin materials, Prog. Polym. Sci. 46 (2015) 86–110.

[3] C. Acharya, S.K. Ghosh, S.C. Kundu, Silk fibroin protein from mulberry and non-mulberry silkworms: cytotoxicity, biocompatibility and kinetics of L929 murine fibroblast adhesion, Journal of Materials Science-Materials in Medicine 19 (2008) 2827–2836.

[4] Y.M. Yang, X.M. Chen, F. Ding, P.Y. Zhang, J. Liu, X.S. Go, Biocompatibility evaluation of silk fibroin with peripheral nerve tissues and cells in vitro, Biomaterials 28 (2007) 1643–1652.

[5] X. Tang, F. Ding, Y.M. Yang, N. Hu, H. Wu, X.S. Gu, Evaluation on in vitro biocompatibility of silk fibroin-based biomaterials with primarily cultured hippocampal neurons, J. Biomed. Mater. Res. A 91A (2009) 166–174.

[6] J.H. Kim, C.H. Park, O.-J. Lee, J.-M. Lee, J.W. Kim, Y.H. Park, C.S. Ki, Preparation and in vivo degradation of controlled biodegradability of electrospun silk fibroin nanofiber mats, J. Biomed. Mater. Res. A 100A (2012) 3287–3295.

[7] B. Zuo, L. Dai, Z. Wu, Analysis of structure and properties of biodegradable regenerated silk fibroin fibers, J. Mater. Sci. 41 (2006) 3357–3361.

[8] B. Mao, C. Liu, W. Zheng, X. Li, R. Ge, H. Shen, X. Guo, Q. Lian, X. Shen, C. Li, Cyclic cRGDfk peptide and Chlorin e6 functionalized silk fibroin nanoparticles for targeted drug delivery and photodynamic therapy, Biomaterials 161 (2018) 306–320.

[9] F. Mottaghitalab, M. Kiani, M. Farokhi, S.C. Kundu, R.L. Reis, M. Gholami, H. Bardania, R. Dinarvand, P. Geramifar, D. Beild, F. Atyabi, Targeted delivery system based on gemcitabine-loaded silk fibroin nanoparticles for lung Cancer therapy, ACS Appl. Mater. Interfaces 9 (2017) 31600–31611.

[10] X.Y. Bian, P.Y. Wu, H.Z. Sha, H.Q. Qian, Q. Wang, L. Cheng, Y. Yang, M. Yang, B. R. Liu, Anti-EGFR-iRGD recombinant protein conjugated silk fibroin nanoparticles for enhanced tumor targeting and antitumor efficiency, Onco. Targets. Ther. 9 (2016) 3153–3162.

[11] S. Gou, Y. Huang, Y. Wan, Y. Ma, X. Zhou, X. Tong, J. Huang, Y. Kang, G. Pan, F. Dai, B. Xiao, Multi-bioresponsive silk fibroin-based nanoparticles with on-demand cytoplasmic drug release capacity for CD44-targeted alleviation of ulcerative colitis, Biomaterials 212 (2019) 39–54.

[12] A. Rodriguez-Nogales, F. Algieri, L. De Matteis, A.A. Lozano-Perez, J. Garrido-Mesa, T. Vezza, J.M. de la Fuente, J.L. Cenis, J. Galvez, M.E. Rodriguez-Cabezas, Intestinal anti-inflammatory effects of RGD-functionalized silk fibroin nanoparticles in trinitrobenzenesulfonic acid-induced experimental colitis in rats, Int. J. Nanomedicine 11 (2016) 5945–5958.

[13] E. Bari, M. Serra, M. Paolillo, E. Bernardi, S. Tengattini, F. Piccinini, C. Lanni, M. Sorlini, G. Bisbano, E. Calleri, M.L. Torre, S. Perteghella, Silk fibroin nanoparticle functionalization with Arg-Gly-asp Cyclopentapeptide promotes active targeting for tumor site-specific delivery, Cancers 13 (2021).

[14] V. Pirota, G. Bisbano, M. Serra, M.L. Torre, F. Doria, E. Bari, M. Paolillo, cRGD-functionalized silk fibroin nanoparticles: a strategy for cancer treatment with a potent unselective naphthalene diimide derivative cancers 15 (2023) 1725.

[15] Y.Q. Zhang, Applications of natural silk protein sericin in biomaterials, Biotechnol. Adv. 20 (2002).

[16] M. Elahi, S. Ali, H.M. Tahir, R. Mushtaq, M.F. Bhatti, Sericin and fibroin nanoparticles-natural product for cancer therapy: a comprehensive review, International Journal of Polymeric Materials and Polymeric Biomaterials 70 (2021) 256–269.

[17] E. Bari, F. Ferrera, T. Altosole, S. Perteghella, P. Mauri, R. Rossi, G. Passignani, L. Mastracci, M. Galati, G.I. Astone, M. Mastrogiacomo, P. Castagnola, D. Fenoglio, D. Di Silvestre, M.L. Torre, G. Filaci, Trojan-horse silk fibroin nanocarriers loaded with a re-call antigen to redirect immunity against cancer, J. Immunother. Cancer 11 (2023).

[18] H. Maeda, The link between infection and cancer: tumor vasculature, free radicals, and drug delivery to tumors via the EPR effect, Cancer Sci. 104 (2013) 779–789.

[19] E. Bari, From Bench to Bedside: The Long Way Towards GMP Scale-Up, Preclinical and Clinical Trials for Silk-based Drug Delivery Systems, Silk-Based Drug Delivery Systems, 2021, pp. 179–204.

[20] A. Giorello, A. Nicastro, C.L.A. Berli, Microfluidic platforms for the production of nanoparticles at flow rates larger than one liter per hour, Advanced Materials Technologies 7 (2022).

[21] J. Ahn, J. Ko, S. Lee, J. Yu, Y. Kim, N.L. Jeon, Microfluidics in nanoparticle drug delivery; From synthesis to pre-clinical screening, Advanced Drug Delivery Reviews 128 (2018) 29–53.

[22] S.J. Shepherd, D. Issadore, M.J. Mitchell, Microfluidic formulation of nanoparticles for biomedical applications, Biomaterials 274 (2021).

[23] K. Osouli-Bostanabad, S. Puliga, D. Serrano, A. Bucchi, G. Halbert, A. Lalatsa, Microfluidic manufacture of lipid-based nanomedicines, Pharmaceutics 14 (2022).

[24] H. Zhang, X. Ma, C. Cao, M. Wang, Y. Zhu, Multifunctional iron oxide/silk-fibroin (Fe3O4-SF) composite microspheres for the delivery of cancer therapeutics, RSC Adv. 4 (2014) 41572–41577.

[25] Z.H. Zhao, Z.J. Zhou, J.F. Bao, Z.Y. Wang, J. Hu, X.Q. Chi, K.Y. Ni, R.F. Wang, X. Y. Chen, Z. Chen, J.H. Gao, Octapod iron oxide nanoparticles as high-performance T-2 contrast agents for magnetic resonance imaging, Nat. Commun. 4 (2013).

[26] H. Wu, S. Zhang, J. Zhang, G. Liu, J. Shi, L. Zhang, X. Cui, M. Ruan, Q. He, W. Bu, A. Hollow-Core, Magnetic, and mesoporous double-shell nanostructure: in situ decomposition/reduction synthesis, bioimaging, and drug-delivery properties, Advanced Functional Materials 21 (2011) 1850–1862.

[27] X. Shi, S.H. Wang, S.D. Swanson, S. Ge, Z. Cao, M.E. Van Antwerp, K.J. Landmark, J.R. Baker Jr., Dendrimer-functionalized shell-crosslinked iron oxide nanoparticles for in-vivo magnetic resonance imaging of tumors, Adv. Mater. 20 (2008) 1671–+.

[28] J.L. Arias, L.H. Reddy, P. Couvreur, Fe3O4/chitosan nanocomposite for magnetic drug targeting to cancer, J. Mater. Chem. 22 (2012) 7622–7632.

[29] P. Kucheryavy, J. He, V.T. John, P. Maharjan, L. Spinu, G.Z. Goloverda, V. L. Kolesnichenko, Superparamagnetic Iron oxide nanoparticles with variable size and an Iron oxidation state as prospective imaging agents, Langmuir 29 (2013) 710–716.

[30] X. Song, H. Gong, S. Yin, L. Cheng, C. Wang, Z. Li, Y. Li, X. Wang, G. Liu, Z. Liu, Ultra- small Iron oxide doped Polypyrrole nanoparticles for in vivo multimodal imaging guided Photothermal therapy, Adv. Funct. Mater. 24 (2014) 1194–1201.

[31] L.-S. Lin, Z.-X. Cong, J.-B. Cao, K.-M. Ke, Q.-L. Peng, J. Gao, H.-H. Yang, G. Liu, X. Chen, Multifunctional Fe3O4@Polydopamine Core-Shell nanocomposites for intracellular mRNA detection and imaging-guided Photothermal therapy, ACS Nano 8 (2014) 3876–3883.

[32] A. Jordan, P. Scholz, P. Wust, H. Fahling, R. Felix, Magnetic fluid hyperthermia (MFH): Cancer treatment with AC magnetic field induced excitation of biocompatible superparamagnetic nanoparticles, J. Magn. Magn. Mater. 201 (1999) 413–419.

[33] H.S. Huang, J.F. Hainfeld, Intravenous magnetic nanoparticle cancer hyperthermia, Int. J. Nanomedicine 8 (2013) 2521–2532.

[34] S. Haracz, M. Hilgendorff, J.D. Rybka, M. Giersig, Effect of surfactant for magnetic properties of iron oxide nanoparticles, nuclear instruments & methods in physics research section b-beam interactions with materials and atoms 364 (2015) 120–126.

[35] A.C. Silva, T.R. Oliveira, J.B. Mamani, S.M.F. Malheiros, L. Malavolta, L.F. Pavon, T.T. Sibov, E. Amaro, A. Tannus, E.L.G. Vidoto, M.J. Martins, R.S. Santos, L. F. Gamarra, Application of hyperthermia induced by superparamagnetic iron oxide nanoparticles in glioma treatment, Int. J. Nanomedicine 6 (2011) 591–603.

[36] Q. Liu, L.B. Feng, Z.L. Chen, Y. Lan, Y. Liu, D. Li, C.G. Yan, Y.K. Xu, Ultrasmall superparamagnetic Iron oxide labeled silk fibroin/hydroxyapatite multifunctional scaffold loaded with bone marrow-derived mesenchymal stem cells for bone regeneration, Front. Bioeng. Biotechnol. 8 (2020).

[37] M. Deng, Z.B. Huang, Y.W. Zou, G.F. Yin, J. Liu, J.W. Gu, Fabrication and neuron cytocompatibility of iron oxide nanoparticles coated with silk-fibroin peptides, Colloids and Surfaces B-Biointerfaces 116 (2014) 465–471.

[38] B. Crivelli, E. Bari, S. Perteghella, L. Catenacci, M. Sorrenti, M. Mocchi, S. Farago, G. Tripodo, A. Prina-Mello, M.L. Torre, Silk fibroin nanoparticles for celecoxib and curcumin delivery: ROS-scavenging and anti-inflammatory activities in an in vitro model of osteoarthritis, Eur. J. Pharm. Biopharm. 137 (2019) 37–45.

[39] D. Caccavo, An overview on the mathematical modeling of hydrogels' behavior for drug delivery systems, Int. J. Pharm. 560 (2019) 175–190.

[40] W.K. Qu, P. Ji, X.B. Han, X.L. Wang, Y. Li, J. Liu, Highly biocompatible Apigenin-loaded silk fibroin Nanospheres: preparation, characterization, and anti-breast-Cancer activity, Polymers 15 (2023).

[41] T. Deptuch, K. Penderecka, M. Kaczmarek, S. Molenda, H. Dams-Kozlowska, In vivo study of the immune response to bioengineered spider silk spheres, Sci. Rep. 12 (2022).

[42] A.A. Lozano-Perez, A. Rodriguez-Nogales, V. Ortiz-Cullera, F. Algieri, J. Garrido-Mesa, P. Zorrilla, M.E. Rodriguez-Cabezas, N. Garrido-Mesa, M.P. Utrilla, L. De Matteis, J.M. de la Fuente, J.L. Cenis, J. Galvez, Silk fibroin nanoparticles constitute a vector for controlled release of resveratrol in an experimental model of inflammatory bowel disease in rats, Int. J. Nanomedicine 9 (2014) 4507–4520.

[43] P. Bourrinet, H.H. Bengele, B. Bonnemain, A. Dencausse, J.M. Idee, P.M. Jacobs, J. M. Lewis, Preclinical safety and pharmacokinetic profile of ferumoxtran-10, an ultrasmall superparamagnetic iron oxide magnetic resonance contrast agent, Invest. Radiol. 41 (2006) 313–324.

[44] S. Zanganeh, G. Hutter, R. Spitler, O. Lenkov, M. Mahmoudi, A. Shaw, J. S. Pajarinen, H. Nejadnik, S. Goodman, M. Moseley, L.M. Coussens, H.E. Daldrup-Link, Iron oxide nanoparticles inhibit tumour growth by inducing pro-inflammatory macrophage polarization in tumour tissues, Nat. Nanotechnol. 11 (2016) 986–994.

[45] A. Kader, J.O. Kaufmann, D.B. Mangarova, J. Moeckel, J. Brangsch, L.C. Adams, J. Zhao, C. Reimann, J. Saatz, H. Traub, R. Buchholz, U. Karst, B. Hamm, M. R. Makowski, Iron oxide nanoparticles for visualization of prostate Cancer in MRI, Cancers 14 (2022).

[46] R.M. Yang, C.P. Fu, N.N. Li, L. Wang, X.D. Xu, D.Y. Yang, J.Z. Fang, X.Q. Jiang, L. M. Zhang, Glycosaminoglycan-targeted iron oxide nanoparticles for magnetic resonance imaging of liver carcinoma, Materials Science & Engineering C-Materials for Biological Applications 45 (2014) 556–563.

[47] J. Gang, S.B. Park, W. Hyung, E.H. Choi, J. Wen, H.S. Kim, Y.G. Shul, S. Haam, S. Y. Song, Magnetic poly ε-caprolactone nanoparticles containing Fe3O4 and gemcitabine enhance anti-tumor effect in pancreatic cancer xenograft mouse model, J. Drug Target. 15 (2007) 445–453.

[48] J.L. Arias, L.H. Reddy, M. Othman, B. Gillet, D. Desmaële, F. Zouhiri, F. Dosio, R. Gref, P. Couvreur, Squalene based nanocomposites: a new platform for the Design of Multifunctional Pharmaceutical Theragnostics, ACS Nano 5 (2011) 1513–1521.

[49] K. Kendall, C. Stainton, Adhesion and aggregation of fine particles, Powder Technol. 121 (2001) 223–229.

[50] M.G. Montalban, J.M. Coburn, A.A. Lozano-Perez, J.L. Cenis, G. Villora, D. L. Kaplan, Production of curcumin-loaded silk fibroin nanoparticles for Cancer therapy, Nanomaterials 8 (2018).

[51] H. Rahmani, A. Fattahi, K. Sadrjavadi, S. Khaledian, Y. Shokoohinia, Preparation and characterization of silk fibroin nanoparticles as a potential drug delivery system for 5-fluorouracil, Advanced Pharmaceutical Bulletin 9 (2019) 601–608.

[52] Z. Zhao, Y. Li, Y. Zhang, A. Chen, G. Li, J. Zhang, M. Xie, Development of silk fibroin modified poly(L-lactide)-poly(ethylene glycol)-poly(L-lactide) nanoparticles in supercritical CO2, Powder Technol. 268 (2014) 118–125.

[53] A.A. Lozano-Perez, H.C. Rivero, M.D.P. Hernandez, A. Pagan, M.G. Montalban, G. Villora, J.L. Cenis, Silk fibroin nanoparticles: efficient vehicles for the natural antioxidant quercetin, Int. J. Pharm. 518 (2017) 11–19.

[54] M. Farahmandjou, F. Soflaee, Synthesis and characterization of alpha-Fe2O3 nanoparticles by simple co-precipitation method, Physical Chemistry Research 3 (2015) 193–198.

[55] H. Kgomo, S. Ncube, V. Mhuka, T.G. Kebede, S. Dube, M.M. Nindi, A comparative study on the dissolution of *Argema mimosae* silk fibroin and fabrication of films and nanofibers, Polymers 13 (2021).

[56] Z.S. Hu, T. Feng, X.L. Zeng, S. Janaswamy, H. Wang, O. Campanella, Structural characterization and digestibility of curcumin loaded Octenyl succinic nanoparticles, Nanomaterials 9 (2019).

[57] P. Ritger, N. Peppas, A simple equation for description of solute release I. Fickian and non-fickian release from non-swellable devices in the form of slabs, spheres, cylinders or discs, J. Control. Release 5 (1987) 23–36.

[58] P. Ritger, N. Peppas, A simple equation for description of solute release II. Fickian and anomalous release from swellable devices, J. Control. Release 5 (1987) 37–42.

[59] N.A. Peppas, J.J. Sahlin, A SIMPLE EQUATION FOR THE DESCRIPTION OF SOLUTE RELEASE .3. COUPLING OF DIFFUSION AND RELAXATION, Int. J. Pharm., 57 (1989) 169–172.

[60] J.M. Unagolla, A.C. Jayasuriya, Drug transport mechanisms and in vitro release kinetics of vancomycin encapsulated chitosan-alginate polyelectrolyte microparticles as a controlled drug delivery system, Eur. J. Pharm. Sci. 114 (2018) 199–209.

[61] O. Marques, J. Neves, N.K. Horvat, S. Colucci, C. Guida, M.U. Muckenthaler, Iron-related parameters are altered between C57BL/6N and C57BL/6J *Mus Musculus* wild-type substrains, Hemasphere 3 (2019).

[62] M.G. Fuster, G. Carissimi, M.G. Montalban, G. Villora, Improving anticancer therapy with Naringenin-loaded silk fibroin nanoparticles, Nanomaterials 10 (2020).

[63] M.I.A. Note, Characterisation of polymers using light scattering techniques, Zetasizer Nano Appl. note (2009).

[64] M. Alexander, D.G. Dalgleish, Dynamic light scattering techniques and their applications in food science, Food Biophys. 1 (2006) 2–13.

[65] J. Saikia, M. Yazdimamaghani, S.P.H. Moghaddam, H. Ghandehari, Differential protein adsorption and cellular uptake of silica nanoparticles based on size and porosity, ACS Appl. Mater. Interfaces 8 (2016) 34820–34832.

[66] M. Elsner, H. Herold, S. Müller-Herrmann, H. Bargel, T. Scheibel, Enhanced cellular uptake of engineered spider silk particles, Biomater. Sci. 3 (2015) 543–551.

[67] M. Schierling, E. Doblhofer, T. Scheibel, Cellular uptake of drug loaded spider silk particles, Biomater. Sci. 4 (2016) 1515–1523.

[68] M.F. Maitz, C. Sperling, T. Wongpinyochit, M. Herklotz, C. Werner, F.P. Seib, Biocompatibility assessment of silk nanoparticles: hemocompatibility and internalization by human blood cells, Nanomedicine-Nanotechnology Biology and Medicine 13 (2017) 2633–2642.

[69] Y. Tian, X. Jiang, X. Chen, Z. Shao, W. Yang, Doxorubicin-loaded magnetic silk fibroin nanoparticles for targeted therapy of multidrug-resistant Cancer, Adv. Mater. 26 (2014) 7393–7398.

[70] A. Florczak, A. Mackiewicz, H. Dams-Kozlowska, Cellular uptake, intracellular distribution and degradation of Her2-targeting silk nanospheres, Int. J. Nanomedicine 14 (2019) 6855–6865.

[71] S. Srinivasan, F.O. Vannberg, J.B. Dixon, Lymphatic transport of exosomes as a rapid route of information dissemination to the lymph node, Sci. Rep. 6 (2016).

[72] S. Solomun, J. Totten, T. Wongpinyochit, A. Florence, F. Seib, Manual versus microfluidic-assisted nanoparticle manufacture: impact of silk fibroin stock on nanoparticle characteristics, ACS Biomater Sci. Eng. 6 (2020) 2796–2804.

[73] S. Matthew, R. Rezwan, Y. Perrie, F. Seib, Volumetric scalability of microfluidic and semi-batch silk nanoprecipitation methods, MOLECULES 27 (2022).